Electrochimica Acta 301 (2019) 229–239

Contents lists available at ScienceDirect

Electrochimica Acta

journal homepage: www.elsevier.com/locate/electacta

Enhanced performance of carbon-free intermetallic zinc titanium alloy (Zn-Zn_xTi_y) anode for lithium-ion batteries

Quoc Hai Nguyen [a, b, 1], Nguyen Thanh Hung [a, 1], Sang Joon Park [a], Il Tae Kim [a, **], Jaehyun Hur [a, *]

[a] Department of Chemical and Biological Engineering, Gachon University, Seongnam, Gyeonggi, 13120, Republic of Korea
[b] Department of Chemical Technology, Baria-Vungtau University, Viet Nam

ARTICLE INFO

Article history:
Received 19 December 2018
Received in revised form
22 January 2019
Accepted 29 January 2019
Available online 31 January 2019

Keywords:
Zinc
Titanium
Intermetallic alloy
Carbon-free
Anode
Lithium-ion batteries

ABSTRACT

A carbon-free intermetallic zinc titanium alloy (carbon-free Zn/Ti) anode, comprising active Zn nanoparticles finely dispersed in Zn_xTi_y ($Zn_{0.6}Ti_{0.4}$ and Zn_3Ti) intermetallic buffer, is prepared via a thermal-treatment followed by a high-energy mechanical milling process for a lithium-ion battery (LIB) anode. As a counter-intuitive phenomenon, without the need of a carbon matrix, the carbon-free Zn/Ti alloy exhibits superior cyclic performance (~1064 mAh cm^{-3} of volumetric capacity after 350 cycles), a good rate capability (85% capacity retention at 3 A g^{-1} compared to its capacity at 0.1 A g^{-1}), and a high initial coulombic efficiency (88%). Although the use of hybrid TiC-C matrix as a control sample still affords highly stable cyclic performance and good rate capability, it exhibits a relatively lower capacity than a carbon-free alloy electrode. The enhanced performance of carbon-free Zn/Ti anodes for LIBs is owing to the presence of stable and cohesive Zn_xTi_y intermetallic phases that provide high conductivity and mechanical stability, thereby mitigating the large volume changes of Zn particles during the lithiation/delithiation processes. High-performance Zn-Zn_xTi_y can be seen as a new promising anode for the next-generation energy storage technology.

1. Introduction

Rechargeable lithium-ion batteries (LIBs) remain the most attractive alternative energy storage system owing to their high capacity, long cycle life, and good rate capability [1–3]. Since their first commercial application in 1991, their technologies have continuously evolved to meet the requirements of the rapid growth of emerging technologies such as mobile electronic devices, hybrid electric vehicles, and grid-scale energy storage systems. Therefore, it is essential to explore new electrode materials in order to improve their energy density, rate capability, safety, and affordability [4–6]. Although graphite is currently used as a commercial anode material for LIBs because of its stability and good conductivity, its energy density limitations (low theoretical specific capacity ~372 mAh g^{-1}), low tap density (<1 g cm^{-3}), and the safety issues associated with its low reaction potential need to be addressed [7–10]. Therefore, numerous studies have been dedicated to developing new alternative materials in order to overcome the drawbacks of graphite anodes [9,11–17].

Significant efforts have been devoted to studying new materials with high theoretical capacity, such as Si, SiO_2, Ge, Sn, Sb, and Zn (specifically categorized as Li alloying/dealloying materials) because of their extremely high theoretical capacities (Si: 4400 mAh g^{-1}, SiO_2: 1965 mAh g^{-1}, Ge: 1600 mAh g^{-1}, Sn: 990 mAh g^{-1}, Sb: 660 mAh g^{-1}, and Zn: 410 mAh g^{-1} [18–29]. Of these, its low theoretical gravimetric capacity notwithstanding (~410 mAh g^{-1}), Zn is a promising material owing to the significant benefits of its extremely high tap density (~7.14 g cm^{-3}) and low operating voltage (~0.4 vs Li/Li^+), as well as other beneficial features including low cost, natural abundance, and eco-friendliness. However, Zn alone typically undergoes large volume changes during Li alloying/dealloying, which result in opening cracks and pulverization, leading to poor cycling behavior as with alloying/dealloying materials [30–32].

A common approach to resolve these problems is to introduce appropriate amounts of additional carbon-based materials (e.g., amorphous carbon, carbon nanotube, graphite, and TiC-C) into Zn as they can play the role of a suitable matrix for Zn in such a way that they improve the cycle life because of their high conductivities

* Corresponding author.
** Corresponding author.
E-mail addresses: itkim@gachon.ac.kr (I.T. Kim), jhhur@gachon.ac.kr (J. Hur).
[1] Contributed equally to this work.

https://doi.org/10.1016/j.electacta.2019.01.182
0013-4686/

and excellent mechanical properties [7,27,33]. However, the use of carbon in composite electrodes poses a number of obvious disadvantages: (1) introduction of carbonaceous materials typically decreases the overall Li-storage capacity because of their lower theoretical capacity than Zn, (2) its low tap density (<1 g cm^{-3}) leads to a significant reduction in volumetric capacity [34], and (3) the high initial capacity loss owing to the irreversible reaction of Li^+ ions on the carbon matrix surface [35,36]. Therefore, the development of a new electrode that does not contain a carbon-based matrix could overcome these problems; however, to realize both high capacity and cyclic stability without adding carbon remains a challenge.

One of the strategies to attain this goal is to create an appropriate intermetallic compound that can act as a carbon-free matrix for active materials. This new matrix should be almost electrochemically inert, but should possess high conductivity and mechanical robustness, thereby contributing to cycling stability toward the active material. In this study, we propose a carbon-free Zn/Ti alloy in which Zn is embedded in a carbon-free intermetallic Zn-Ti alloy (Zn_xTi_y) matrix prepared by high energy mechanical milling (HEMM). The beneficial features of Zn_xTi_y are as follows: (1) their strong Zn—Ti bond (large negative heats of formation) inevitably causes an increase in the bulk modulus and a decrease in the average atomic volume that enhances phase stability and cohesive properties, and (2) their high Young's modulus (>100000 MPa) implies good mechanical stability. As a result, we demonstrate the excellent electrochemical performance of Zn/Ti alloy (Zn-Zn_xTi_y) even without the carbon matrix because of the presence of stable and cohesive Zn_xTi_y [37] that can effectively buffer the significant volume expansion of Zn particles during the Li alloying/dealloying processes, as well as enhance the electronic conductivity. In particular, at the optimum atomic ratio (1:1) between Zn and Ti, carbon-free Zn/Ti anodes (Zn/Ti (11)) exhibit excellent cyclic performance (~1064 mAh·cm^{-3} of volumetric capacity after 350 cycles), good rate capability (85% capacity retention at 3 A g^{-1} compared to the capacity at 0.1 A g^{-1}), and high initial coulombic efficiency (88%). In comparison, although Zn/Ti (11) with carbon (namely, Zn/Ti (11)-C or Zn-TiC-C (resulting composite)) also exhibits good stability in cyclic performance, its capacity is significantly lower because of the presence of carbon.

2. Experimental section

2.1. Material preparation

To prepare carbon-free Zn/Ti powders, 2 g mixtures of Zn powder (<10 μm, ≥98%, Aldrich) and Ti powder (325 mesh, 99.99%, Alfa Aesar) at atomic ratios of 1:1 (1.15 g of Zn and 0.85 g of Ti), 2:1 (1.55 g of Zn and 0.45 g of Ti), and 1:3 (0.62 g of Zn and 1.38 g of Ti) were heat-treated at 600 °C for 6 h in an Ar (10 cc min^{-1}) environment after physical mixing. These mixtures (2 g) were then placed in an 80 cm^3 zirconium oxide bowl with zirconium oxide balls (diameters 3/8 in. and 3/16 in.) at a ball-to-powder mass ratio of 20:1 and sealed in an Ar atmosphere. Planetary mechanical milling (Pulverisette 5, Fritsch) was performed at room temperature at 300 rpm for 40 h (repetition of 1 h milling with 30 min break). For the preparation of the Zn-TiC-C composite, the same procedure was applied except that 30 wt% of carbon black (Super P, Alfa Aesar, 99.99%) was added to a mixture of Zn/Ti at the ball-milling stage.

2.2. Material characterization

The resulting electrode powder was characterized by X-ray diffraction (XRD) with an X-ray diffractometer with Cu Kα (λ = 1.5406 nm) radiation (D/MAX-2200 Rigaku, Japan). A micro Raman spectrometer (ANDOR Monora500i, 633 nm) and an X-ray photoelectron spectroscopy (XPS, Kratos AXIS Nova) were used to investigate the structure information of as-prepared powder. The Brunauer-Emmett-Teller (BET) nitrogen adsorption/desorption method (ASAP 2020, Micromeritics, USA) was used to measure the specific areas. A scanning electron microscope (SEM, Hitachi S4700, Japan) and a high-resolution and scanning transmission electron microscope (HRTEM and STEM, TECNAI G2F30) equipped with energy dispersive X-ray (EDX) spectrometry were used to investigate the morphologies, composition, and element analysis of the synthesized samples. *Ex situ* SEM images were obtained to observe the morphology of different electrode materials before and after 50 cycles.

2.3. Electrochemical measurements

Electrochemical performances were measured using CR2032-type coin cells assembled in an Ar-filled glove box, in which a working electrode as an anode and a lithium foil as a counter electrode were separated by a polyethylene membrane, along with 1 M $LiPF_6$ in ethylene carbonate (EC)/diethylene carbonate (DEC) (1:1 by v/v) as an electrolyte solution. The working electrode was prepared by mixing 70 wt% of as-prepared powder, 15 wt% of carbon black, and 15 wt% of binder (polyvinylidene fluoride (PVDF)) in *N*-methyl-pyrrolidone solvent. The mixture was then cast on a copper foil by the doctor blade method followed by drying at 70 °C for 12 h in vacuum. Galvanostatic charge-discharge cycling tests were performed using a battery cycler (WBCS3000, WonAtech) in the range 0.01—2.0 V (vs. Li/Li^+) at a current density of 0.1 A g^{-1}. The total weight of the active material consisting of pure Zn and Zn_xTi_y was used to calculate the gravimetric capacity. The volumetric capacity (with a unit of mAh cm^{-3}) was achieved using the tap density (g cm^{-3}) and measured gravimetric capacity of the powder electrode, in which the tap density was obtained from the measured volume and weight of the powder. The cyclic voltammetrogram (CV) was measured by a ZIVE MP1 multichannel electrochemical workstation (WonAtech) in the range of 0.01—2.0 V at a scanning rate of 0.2 mV s^{-1}. The rate capability was measured at different current densities of 0.1, 0.5, 1, and 3 A g^{-1} using a battery cycler (WBCS3000, WonAtech). Electrochemical impedance spectroscopy (EIS) measurements were performed using a multichannel electrochemical workstation (ZIVE MP1, WonAtech) in the range 100 kHz to 100 mHz.

3. Results and discussion

The XRD patterns of the carbon-free Zn/Ti alloys and Zn-TiC-C are shown in Fig. 1a—c, together with the theoretical peak positions of the Zn, Ti, TiC, Zn_3Ti, and $Zn_{0.6}Ti_{0.4}$ phases in Fig. 1d (PDF#04-0831, PDF#44-1294, PDF#32-1383, PDF#07-0098, and PDF#17-0672, respectively). For the carbon-free Zn/Ti before HEMM (i.e., only after heat-treatment, Fig. 1a), the diffraction peaks can be identified with four phases of Zn, Ti, Zn_3Ti, and $Zn_{0.6}Ti_{0.4}$ that are well-matched with the reference peaks in Fig. 1d, suggesting that the introduction of thermal-treatment before HEMM facilitates the formation of Zn_3Ti and $Zn_{0.6}Ti_{0.4}$ phases; however, a significant amount of Zn and Ti phases remains in the alloy. All peak positions remain unchanged for carbon-free Zn/Ti after HEMM in contrast to that before HEMM, except for the decrease in the peak intensities for the Ti and Zn_3Ti phases and the increase in the peak intensities for the $Zn_{0.6}Ti_{0.4}$ phase (Fig. 1b), indicating transformation from Ti and Zn_3Ti to the $Zn_{0.6}Ti_{0.4}$ phase during HEMM (i.e., the formation of Zn-Zn_xTi_y). However, the main peaks of Zn at ~39° (100) and 43.2°(101) indicates the broadened and decreased intensity after the HEMM

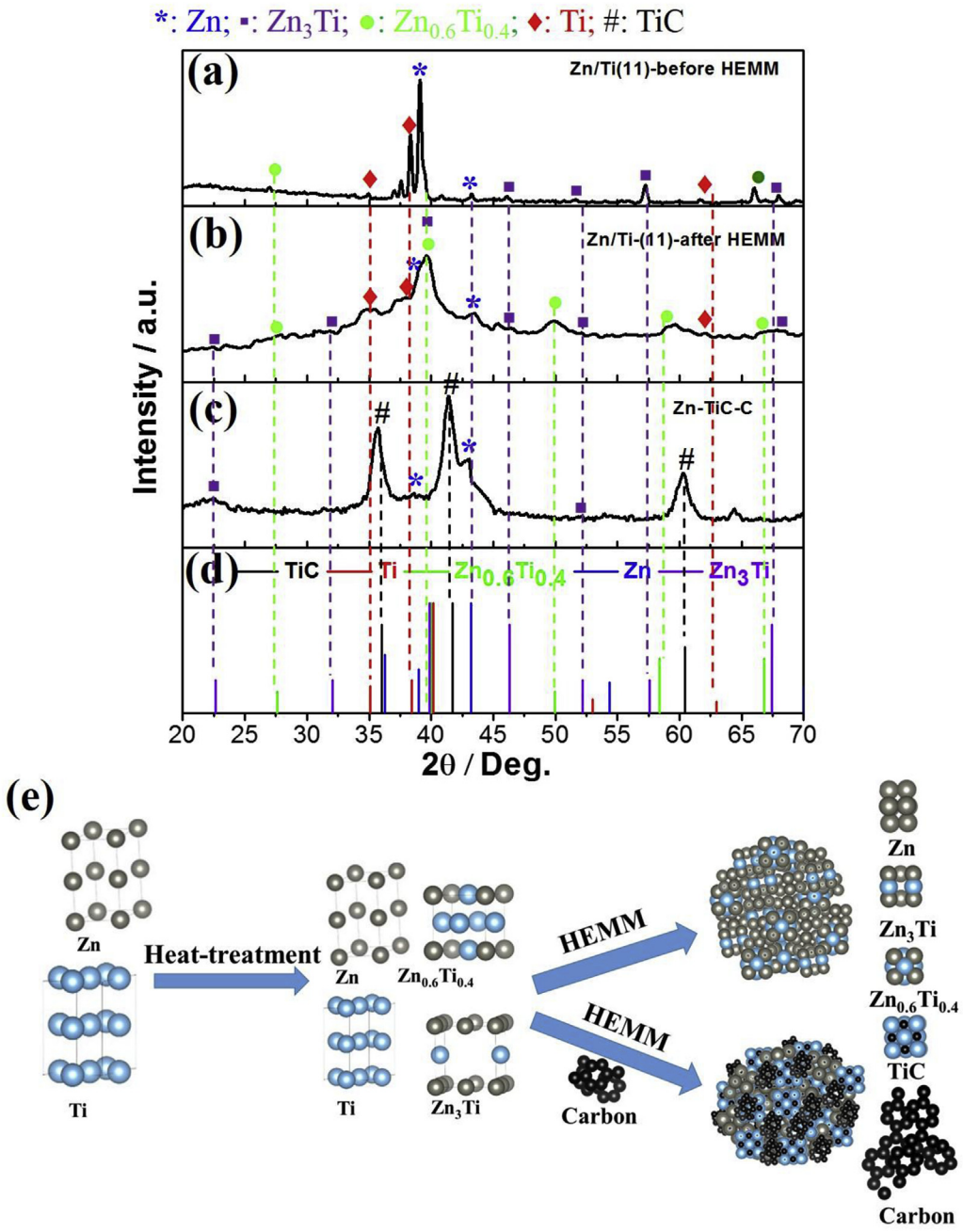

Fig. 1. (a–c) XRD patterns of carbon-free Zn/Ti (11)-before HEMM, Zn/Ti (11)-after HEMM, and Zn-TiC-C. (d) The theoretical XRD data are shown as a reference. (e) Schematic diagram of the fabrication of carbon-free Zn/Ti (11) and Zn-TiC-C.

process, revealing the reduced crystallinity of Zn during HEMM. On the other hand, the peaks observed for the Zn-TiC-C composite (Fig. 1c) are clearly distinct from those of the carbon-free Zn/Ti sample. The peaks found at ~36°, 41.7°, and 60.4° correspond to the theoretical peaks of the TiC phase (PDF#32-1383) with the weak Zn peaks at ~39° and 43.2° (PDF#04-0831), indicating the presence of the conductive TiC phase together with nanosized Zn in the composite (i.e., the formation of Zn-TiC-C). The formation of TiC phase in the presence of free carbon matrix to form the hybrid TiC-C matrix is further confirmed by Raman (Fig. S1) and deconvoluted XPS spectra (Fig. S2). The successful formation of the TiC phase is in good agreement with the previous results obtained with similar approaches [33,38–40]. Minor Zn_3Ti peaks are also observed in the case of Zn-TiC-C, while the peaks of $Zn_{0.6}Ti_{0.4}$ disappear. This could be attributed to the priority of the TiC formation by consuming Ti and carbon rather than the production of $Zn_{0.6}Ti_{0.4}$ for Zn-TiC-C. The overall reactions for carbon-free Zn/Ti and Zn-TiC-C can be summarized as follows, and are shown in Fig. 1e:

$$\text{Carbon}-\text{free Zn/Ti alloys (Zn/Ti): Zn} + \text{Ti} \xrightarrow{\text{Heat}-\text{treatment}} \text{Zn} + \text{Ti} + \text{Zn}_3\text{Ti} + \text{Zn}_{0.6}\text{Ti}_{0.4} \xrightarrow{\text{HEMM}} \text{Zn}-\text{ZnxTiy}(\text{Zn}_{0.6}\text{Ti}_{0.4}(\text{major}) + \text{Zn}_3\text{Ti}(\text{minor})) \quad (1)$$

$$Zn/Ti-C\ \text{composite}(Zn-TiC-C):Zn+Ti \overset{\text{Heat-treatment}}{\rightarrow} Zn + Ti + Zn_3Ti + Zn_{0.6}Ti_{0.4} \overset{\text{HEMM}}{\rightarrow} Zn-TiC-C \quad (2)$$

Comparison of the XRD results for carbon-free Zn/Ti alloys with different atomic ratios (1:1, 2:1, and 1:3, hereafter, denoted as Zn/Ti (11), Zn/Ti (21), and Zn/Ti (13), respectively) after HEMM are shown in Fig. 1b and Fig. S3. Compared to the carbon-free Zn/Ti (11) (Fig. 1b), the existence of Ti (red) and $Zn_{0.6}Ti_{0.4}$ (green) phases becomes more pronounced in the case of the highest Ti content (ZnTi/(13) (Fig. S3b)), while the Ti (red) and $Zn_{0.6}Ti_{0.4}$ (green) peaks are significantly reduced in the case of the smallest Ti content (Zn/Ti (21) (Fig. S3a)). Because pure Ti is inactive to the Li^+ ion storage, a high content of Ti (i.e., for Zn/Ti (13)) can reduce the specific capacity of the electrode. However, excessive Zn content (i.e., for Zn/Ti (21)) can lead to poor cycling behavior because of the insufficient amount of inactive components (Ti and $Zn_{0.6}Ti_{0.4}$) that cannot sufficiently prevent the large volume changes of Zn particles during the cycling.

The SEM micrographs of the as-prepared carbon-free Zn/Ti alloys with three different ratios (Zn/Ti (21), Zn/Ti (11), and Zn/Ti (13)) are shown in Fig. 2a–c, together with that of the Zn-TiC-C composite (Fig. 2d). Of interest is that the average particle sizes of carbon-free Zn/Ti alloys depend on the Zn content, with increasing particle size and increasing Zn content (Fig. 2a–c). This could be attributed to the greater probability of melting and agglutability of Zn (melting temperature of 420 °C) than Ti (melting temperature of 1668 °C) during HEMM. In addition, the significant reduction in the average particle size for Zn-TiC-C is because of the continuous fracture and welding of powders with significantly strong TiC phases [7,33]. Although the average particle sizes are relatively large (mostly < 5 μm) for both Zn/Ti (11) and Zn/Ti (13) compared with that of Zn-TiC-C (mostly < 1 μm), they are still significantly smaller than that of Zn/Ti (21) (primarily > 10 μm) (Fig. 2e), indicating the greater surface area of Zn/Ti (11) and Zn/Ti (13) than that of Zn/Ti (21). Also, from the BET analyses for pure Zn, Zn/Ti (11), and Zn-TiC-C in Fig. 2f, Zn-TiC-C shows the highest surface area, followed by Zn/Ti (11) and pure Zn.

Fig. 3 shows the HRTEM and STEM with EDS mapping images of

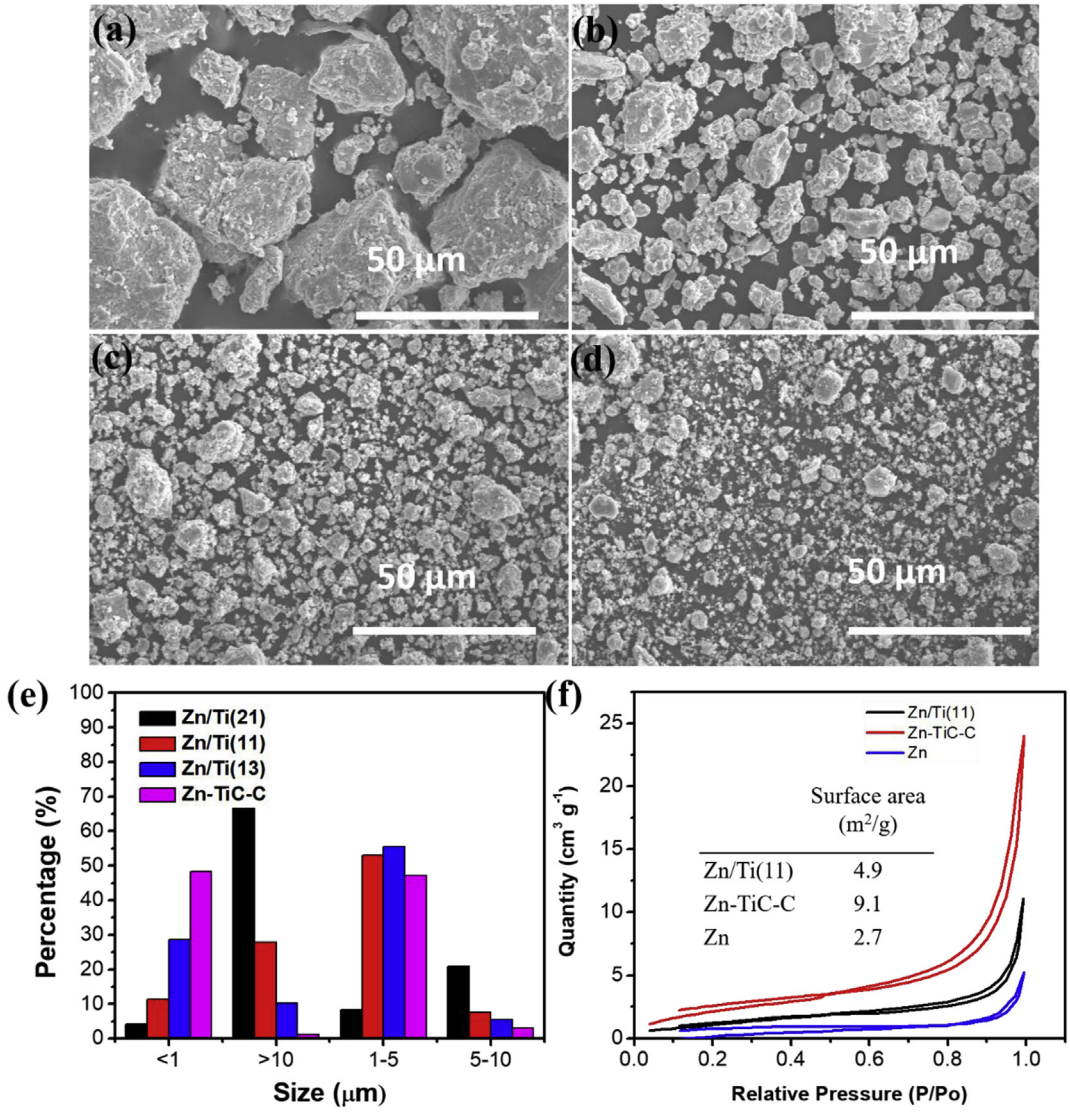

Fig. 2. SEM images of (a) Zn/Ti (21), (b) Zn/Ti (11), (c) Zn/Ti (13), and (d) Zn-TiC-C. (e) Particle size distribution of carbon-free Zn/Ti alloys and Zn-TiC-C composite. (f) BET results of carbon-free Zn/Ti (11), Zn-TiC-C, and pure Zn.

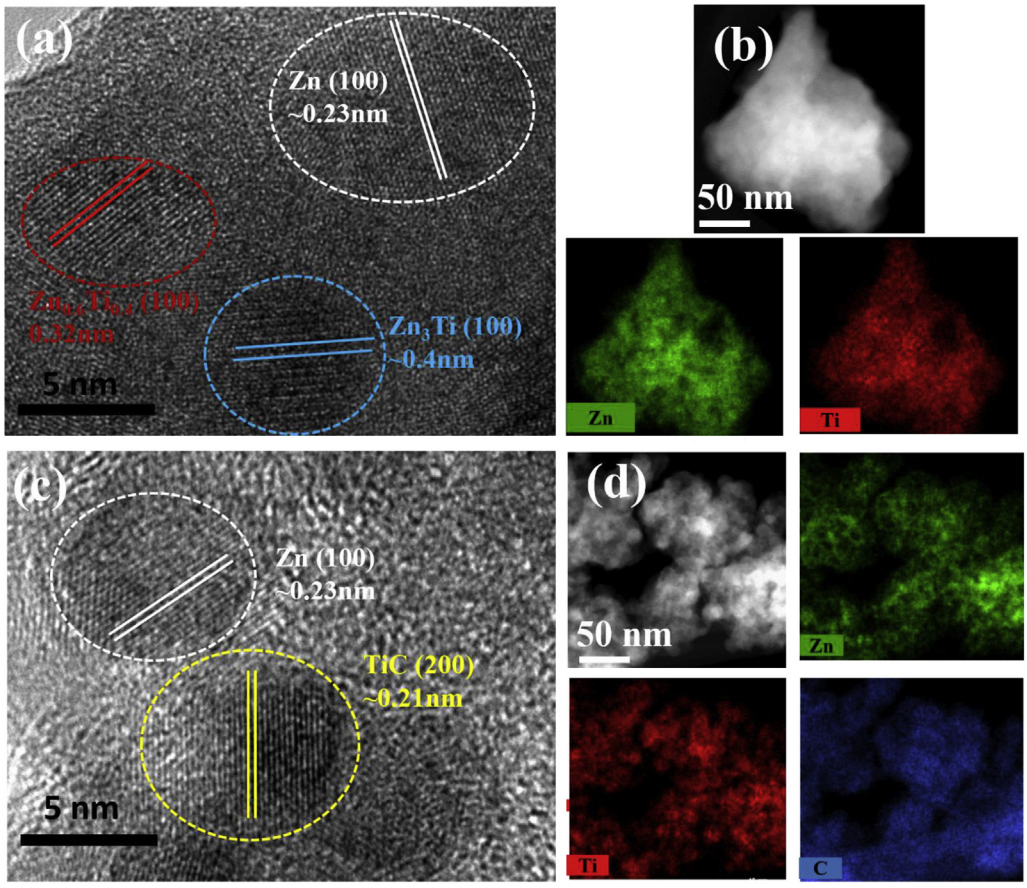

Fig. 3. High-resolution TEM and STEM images along with EDS mapping images for each element of (a–b) carbon-free Zn/Ti (11) alloy and (c–d) Zn-TiC-C composite.

each element (Ti: red; Zn: green; and C: blue) for carbon-free Zn/Ti (11) alloy (Fig. 3a and b) and Zn-TiC-C composite (Fig. 3c and d). As can be seen in the HRTEM images, the carbon-free Zn/Ti (11) alloy (Fig. 3a) displays Zn (100), Zn_3Ti (100), and $Zn_{0.6}Ti_{0.4}$ (100) phases corresponding to lattice plane separations of ~0.23, 0.4, and 0.32 nm, respectively, which are homogeneously dispersed in the alloy. However, the Zn-TiC-C composite (Fig. 3c) exhibits the lattice fringes of Zn (~0.23 nm) and TiC (~0.21 nm) corresponding to the (100) plane for Zn and (200) plane for TiC, which are consistent with the XRD results. Additionally, the STEM and EDS mapping images of both carbon-free Zn/Ti (11) (Fig. 3b) and Zn-TiC-C further confirm the homogeneous distribution of Zn and Ti throughout a large area. The crystallite sizes of Zn, Zn_3Ti, and $Zn_{0.6}Ti_{0.4}$ phases are estimated to be smaller than 10 nm, which is in good agreement with the domain sizes obtained from the Scherrer equation based on XRD analysis ($d = 0.9 \times \lambda/(\beta \cos(\theta))$, where λ is X-ray wavelength (0.15406 nm), β is the line broadening at half the maximum intensity (FWHM), and θ is the Bragg angle (where 2θs are ~39°, 22.6°, and 27.6° for Zn (110), Zn_3Ti (100), and $Zn_{0.6}Ti_{0.4}$ (100), respectively).

Fig. 4a shows the initial charge/discharge profiles of carbon-free Zn/Ti (11), Zn-TiC-C, and pure Zn electrodes at a constant current density of 0.1 A g^{-1}. As can be seen in Fig. 4a, these electrodes exhibit initial discharge/charge capacities of ~607/535, 574/411, and 488/228 mAh g^{-1}/mAh g^{-1} corresponding to the initial coulombic efficiencies (ICEs) of ~88%, 72%, and 47%, respectively. The initial capacity loss is caused primarily by the irreversible reaction of Zn with Li and a subreaction between electrolytes and the electrode surface. Therefore, the lowest ICE of pure Zn electrode could be attributed to the absence of the buffering matrix that can mitigate the volume changes of Zn. However, the introduction of buffering Zn_xTi_y, or the TiC-C phase for carbon-free Zn/Ti (11) alloy or for Zn-TiC-C composite, significantly suppresses the volume change of active Zn, resulting in improved ICEs of these electrodes. On the other hand, the initial capacity loss of Zn-TiC-C is greater than that of carbon-free Zn/Ti (11) because of the irreversible reaction of Li with free carbon (that could be confirmed by Raman and XPS results in Fig. S1 and Fig. S2, respectively) and the subreaction that are significantly decreased in the case of carbon-free Zn/Ti (11). After the 1st cycle, excellent CEs are observed for the carbon-free Zn/Ti (11) (with 95% and 96%), for Zn-TiC-C (with 97% and 95%) for the second and third cycles, respectively, as shown in Fig. S4a and Fig. S4b, which could be attributed to the existence of stable Zn_xTi_y phases and TiC-C hybrid matrix that accommodate volume changes of Zn particles during repeated cycling as compared to the poor CEs for pure Zn electrode (with 93% and 88% for the second and third cycle, respectively (Fig. S4c). The initial discharge capacities of all samples are typically greater than their calculated theoretical capacities. This is associated with the formation of the solid electrolyte interface (SEI) layer on the surface of the Zn particles and side reactions from impurities during the initial stage of the electrochemical reaction [7,33].

To better understand the electrochemical reaction mechanisms of Zn, Zn-TiC-C, and carbon-free Zn/Ti (11), cyclic voltammograms (CVs) were plotted for the first three cycles, as shown in Fig. 4b–d. During the first discharge process of the pure Zn electrode (Fig. 4b), the small peak at ~0.65 V corresponds to the formation of the SEI layer on the surface of Zn, while the two larger peaks at ~0.35

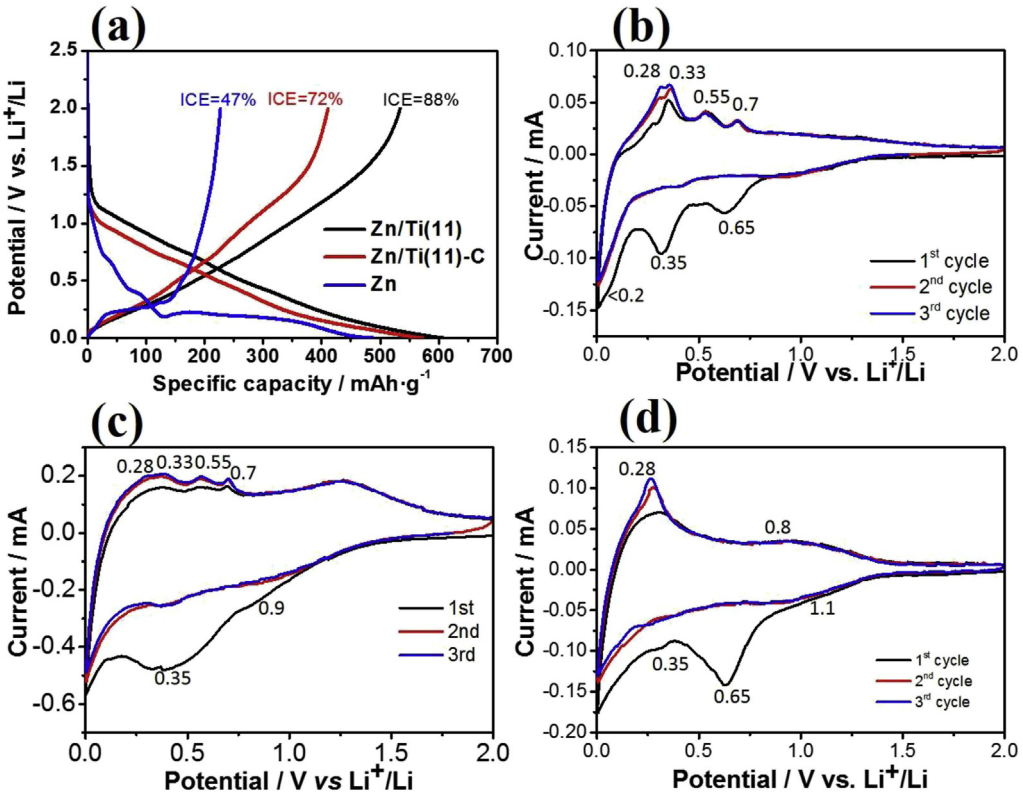

Fig. 4. (a) Initial voltage profile and (b–d) cyclic voltammetry plots of pure Zn, Zn-TiC-C, and carbon-free Zn/Ti (11).

and < 0.2 V are associated with the sequential lithiation reactions of Li with Zn to form the LiZn phase (Zn → $LiZn_4$ → LiZn) [27,33]. In the 1st charge, two large peaks at ~0.28 and ~0.33 V and two small peaks at ~0.55 and ~0.7 V are observed, which are matched with a series of delithiation processes (LiZn → $LiZn_2$ → αLi_2Zn_5 → $\alpha LiZn_4$ → Zn) [27]. In the subsequent discharge/charge processes, the SEI peaks disappear and the lithiation/delithiation peaks remain sharp except for the significant reduction in their intensities. In the case of Zn-TiC-C, similar behaviors to the Zn electrode are exhibited, except for an additional peak at ~0.9 V corresponding to the formation of an SEI layer on the surface of the carbon [41] (Fig. 4c). The initial capacity of Zn-TiC-C is greater than that of pure Zn (574 mAh g^{-1} compared to 488 mAh g^{-1}), in all probability because of the greater surface area, as shown in Fig. 2f. Although the introduction of carbonaceous materials typically decreases the overall Li-storage capacity because of the reduced content of active material (Zn in this case), the pure Zn electrode showed the lower specific capacity than Zn-TiC-C due to much smaller surface area (2.7 m^2 g^{-1} for pure Zn compared to 9.1 m^2 g^{-1} for Zn-TiC-C) and much bigger particle sizes that prevent the complete reaction between active Zn and Li ions, thereby reducing the initial Li-storage capacity. On the other hand, upon comparing Zn/Ti (11)-C and Zn/Ti (11), the capacity of Zn/Ti (11) is higher than that of Zn/Ti (11)-C in which the concentration of active material might have played a major role in increasing the capacity because the surface area of Zn/Ti (11) was lower than that of Zn/Ti (11)-C (Fig. 2f). Overall, the capacity contribution from carbon should be understood considering many different factors such as surface area (or particle size) and concentration of active material (or theoretical capacity) together. However, all lithiation/delithiation peaks become smeared as the Zn nanocrystallites are well dispersed in the TiC-C matrix during the HEMM [7]. In addition, from the 2nd cycle the SEI peak at ~0.9 V disappear and all other peaks retained their positions and intensities, indicating the stabilized electrochemical reactions of Zn with Li^+ because of the existence of the TiC-C matrix [7,33,38–40]. Remarkably, in the case of the carbon-free Zn/Ti (11) electrode (Fig. 4d), apart from one peak that appeared at ~1.1 V that could be attributed to the SEI layer formation on the surface of Zn_xTi_y phases, all other peaks are observed to be in good agreement with the case of pure Zn because of the presence of active Zn particles in the Zn_xTi_y matrix. After the 1st cycle, the reduction peak at ~0.35 V is shifted toward a higher potential because of the reduced polarization during the discharge process, whereas the oxidation peaks are typically overlapped with little change in their intensities, indicating the highly stabilized electrochemical reactions after the 1st cycle.

For a better understanding of the Li storage mechanism of the Zn/Ti (11) electrode during cycling, *ex situ* XRD measurements were conducted by opening the cells at the fully lithiated and delithiated along with pristine stage, as shown in Fig. 5a. For pristine Zn/Ti (11) electrode, the crystalline phases observed (Zn, $Zn_{0.6}Ti_{0.4}$, and Zn_3Ti, together with two prominent peaks of copper foil) are typically consistent with the XRD results for as-prepared powder (Fig. 1b), except for their reduced intensities as the *ex situ* XRD measurements were performed on the electrode material comprising additional conductive carbon and PVDF binder as well as active material (Zn/Ti (11)). In the fully lithiated at 0.01 V, five new peaks at ~21, 24, 48, 60.5, 65.5°, corresponding to LiZn phase, were observed together with the remained peaks of $Zn_{0.6}Ti_{0.4}$, Zn_3Ti, and Cu, while the main peak of Zn at ~43.5° showed the significant reduction in intensity. This indicates that most of Zn reacted with Li to form Li-Zn alloy during the discharge process, which are in good agreement with results of Hwa et al. [27]. On the other hand, after complete delithiation at 2.0 V, the peak intensity of Zn at ~43.5° recovered to approximately that of the pristine stage. In addition, the peaks of the Li-Zn alloy disappears at the full-charged stage,

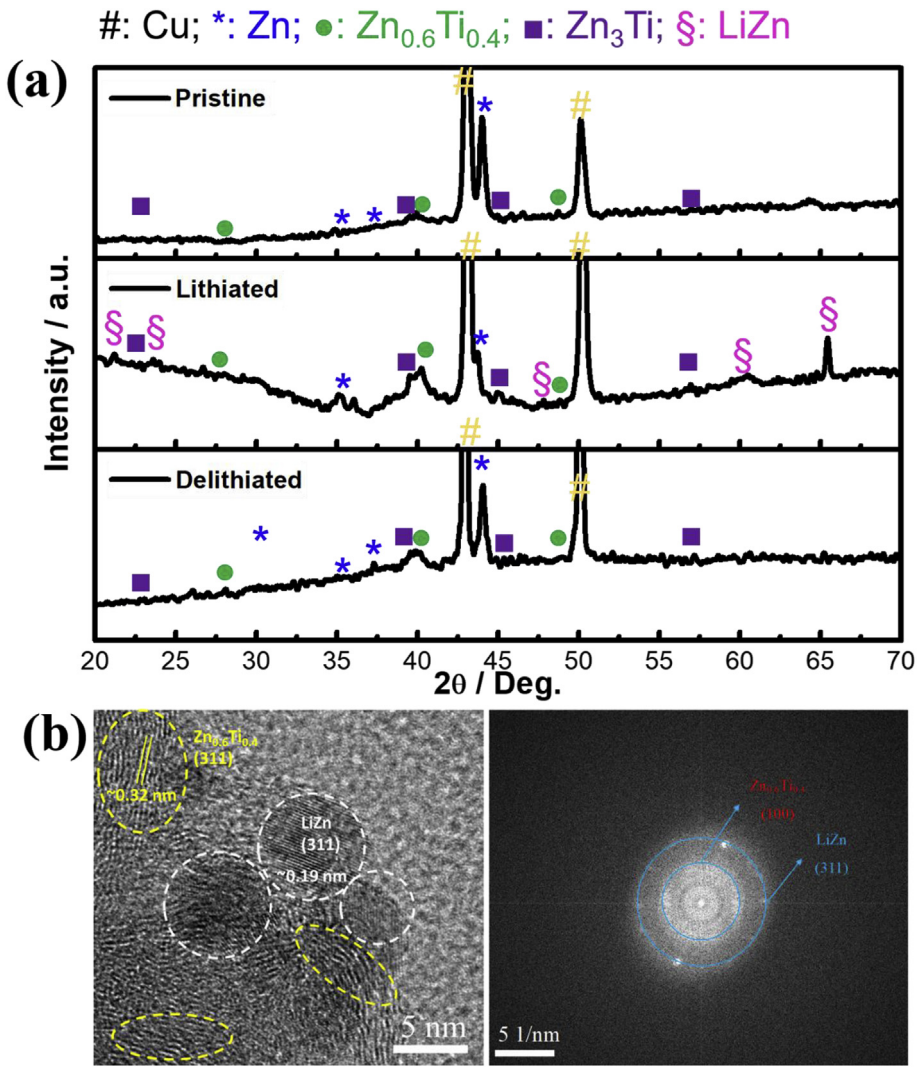

Fig. 5. *Ex situ* XRD patterns of carbon-free Zn/Ti (11) electrode at fully lithiated and delithiated state along with pristine stage. (b) *Ex-situ* HRTEM image and SEAD patterns of carbon-free Zn/Ti (11) at fully lithiated state.

which demonstrates the complete reversibility of LiZn to the Zn phase. In addition, the $Zn_{0.6}Ti_{0.4}$ and Zn_3Ti peaks remains unchanged throughout the discharge/charge process as well as pristine stage, indicating electrochemical inertness and acting as a conductive matrix for Zn. *Ex-situ* HRTEM image and SAED pattern of Zn/Ti (11) at fully lithiated process was further investigated in Fig. 5b. This results display LiZn (311) phase corresponding to the lattice plane separation of ~0.19 nm beside the presence of $Zn_{0.6}Ti_{0.4}$ phase ((311) plane corresponding to ~0.32 nm), which are fully consistent with *ex-situ* XRD result in Fig. 5a.

Fig. 6a compares the cyclic performances of the carbon-free Zn/Ti (11), Zn-TiC-C and pure Zn electrodes based on the gravimetric capacities and Fig. 6b illustrates the volumetric capacities of the carbon-free Zn/Ti (11), Zn-TiC-C and pure Zn electrodes. Despite their high initial gravimetric capacities (607, 574, and 488 mAh g^{-1} for carbon-free Zn/Ti (11), Zn-TiC-C and pure Zn, respectively), they exhibit distinct behavior after the second cycle. The specific capacity rapidly decays to less than 100 mAh g^{-1} after 15 cycles for pure Zn electrode, which could be ascribed to mechanical cracking and crumbling caused by large volume changes during repeated cycling. In contrast, when the TiC-C matrix is introduced, the Zn-TiC-C electrode exhibits excellent cyclic stability, as even after 350 cycles the specific capacity remained at ~304 mAh g^{-1} (94% of capacity retention compared to the capacity at the 2nd cycle). The enhanced cyclic stability could be attributed to the uniform dispersion of Zn particles in the TiC-C conductive matrix that suppresses particle agglomeration and accommodates the volume expansion of Zn particles during Li alloying [33,38–40,42]. Of significance is that the formation of the Zn_xTi_y phase in the case of carbon-free Zn/Ti (11) also contributes to the enhanced cyclic stability because of its mechanical stability and cohesive properties that could buffer the volume changes of Zn particles during cycling [37], and could even increase the specific capacity compared to that of Zn-TiC-C because of the absence of carbon, as discussed earlier. Therefore, the carbon-free Zn/Ti (11) electrode exhibits the superior cyclic performance with 350 mAh g^{-1} of gravimetric capacity after 350 cycles, which is significantly greater than that of the Zn-TiC-C composite. The XPS result in Fig. S5 presents the signal from Zn deconvoluted into two peaks located at ~1044.8 and ~1021.7 eV corresponding to the Zn $2p_{1/2}$ and Zn $2p_{3/2}$, respectively, confirming the pure Zn. In addition, there are two small peaks detected at ~975 and ~998 eV which might be ascribed to the Zn 2p in the Zn_xTi_y phases (circle in Fig. S5a), while two signals from Ti $2p_{1/2}$ and Ti $2p_{3/2}$ appeared at ~458 and 464 eV, which are higher than those

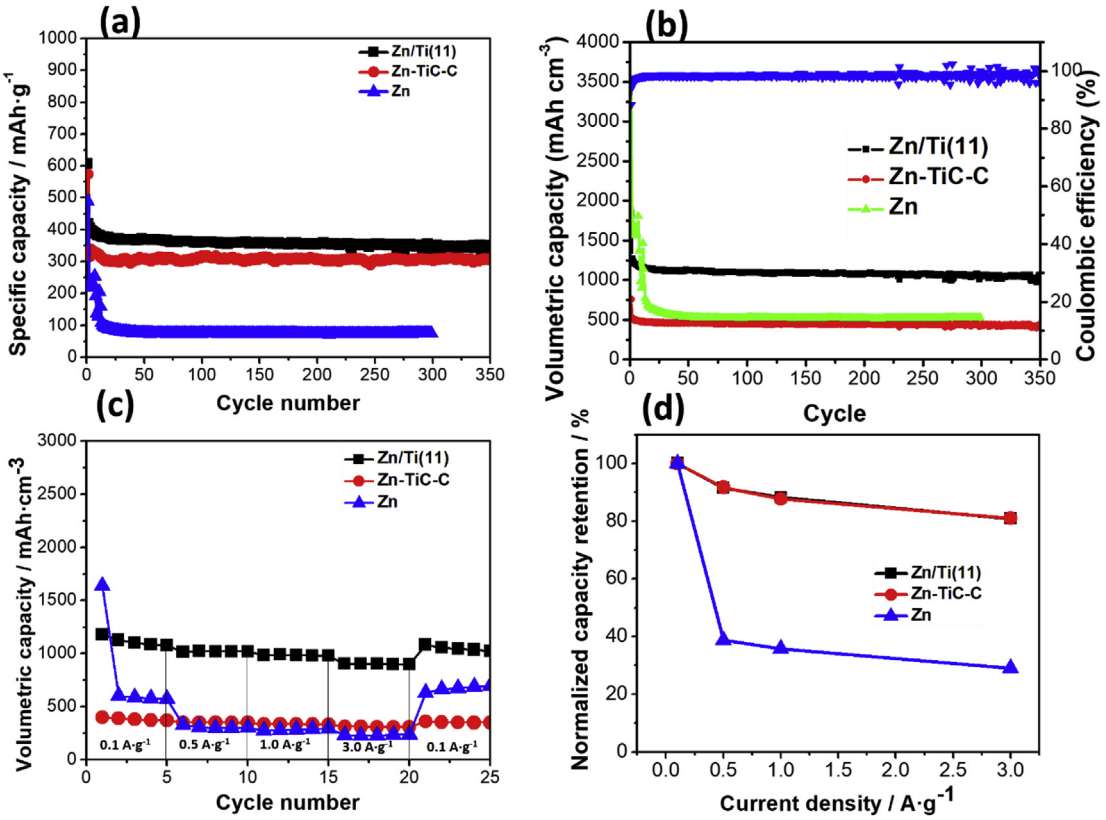

Fig. 6. (a) Long-term cycling performance of carbon-free Zn/Ti (11), Zn-TiC-C, and pure Zn from 0.01 to 2.0 V vs Li^+/Li, (b) Volumetric capacities calculated based on mass and tap density of active material, (c) Rate capability of carbon-free Zn/Ti (11), Zn-TiC-C, and pure Zn at various current densities of 0.1, 0.5, 1,3, and 0.1 A g^{-1}, and (d) Normalized charge capacity retention).

from metallic Ti 2p peaks (~454 and 460 eV), indicating the formation of Zn_xTi_y rather than pure Ti [33]. Owing to the small peaks of Zn 2p in Zn_xTi_y (Fig. S5a), it could be effectively considered negligible. Therefore, the mass percentage of pure Zn was estimated based on the deconvoluted Zn 2p and Ti 2p peaks, which gives 67.54% of pure Zn. Therefore, the theoretical capacity of carbon-free Zn/Ti (11) could be calculated based on wt% of pure Zn in Zn/Ti alloy; that is ~277 mAh g^{-1}. This theoretical capacity of Zn/Ti alloy is lower than the specific capacity (350 mAh g^{-1}) from electrochemical results, which might be attributed to the Li-adsorption in the structure of Zn_xTi_y phases. Due to the formation of Zn_3Ti and $Zn_{0.6}Ti_{0.4}$ phase with lattice plane separation of 0.4 nm and 0.32 nm, respectively, which are similar or even higher than that of graphite (~0.34 nm), the Li-storage mechanisms based on Zn_3Ti and $Zn_{0.6}Ti_{0.4}$ edges surface without any change in structure of Zn_xTi_y could be expected just as in the mechanism of excess Li-storage sites in carbon materials that have been investigated in previous reports [43–46]. In addition, the tap density of carbon-free Zn/Ti (11) increases significantly up to ~3 g cm^{-3} compared to ~1.25 g cm^{-3} for Zn-TiC-C (Table S1), resulting in a significant volumetric capacity of 1064 mAh cm^{-3} after 350 cycles which is over two-fold higher than the volumetric capacities of Zn-TiC-C (430 mAh cm^{-3}) and pure Zn (525 mAh cm^{-3}) (Fig. 6b).

The rate capability and normalized capacity retention of these electrodes at various current densities from 0.1 to 3 A g^{-1} are shown in Fig. 6c and d. The pure Zn electrode exhibits a poor rate capability and delivers a charge capacity of ~231 mAh·cm^{-3} at a current density of 3 A g^{-1}, corresponding to 29% capacity retention compared to the capacity at 0.1 A g^{-1}. In addition, when Zn_xTi_y or TiC-C is introduced, the rate capability is significantly improved to ~900 mAh·cm^{-3} and ~310 mAh cm^{-3} of reversible charge capacities, respectively, corresponding to charge capacity retentions of 81% for both carbon-free Zn/Ti (11) and Zn-TiC-C. The excellent performance of these electrodes could be attributed to the high degree of incorporation of the conductive hybrid TiC-C matrix as well as the Zn_xTi_y intermetallic phases, which promote electron transport in the electrodes and act as an effective buffer that mitigates stress and strain during the cycling. In addition, the greater capacity of the carbon-free Zn/Ti (11) electrode than Zn-TiC-C is consistently confirmed for all current densities (Fig. 6c), which demonstrates the superiority of the Zn_xTi_y alloy to TiC-C. When the rate capability between different metal ratios (Zn:Ti) is compared, the poor performance of Zn/Ti (21) is observed (Fig. S6), which could be attributed to the excessive amount of Zn in Zn/Ti intermetallic compounds that leads to the difficulty in forming the $Zn_{0.6}Ti_{0.4}$ matrix and the greatest particle size (Fig. 2a) than that observed at other ratios (1:1 and 1:3, Fig. 2b and c, respectively). However, in spite of the high cyclic stability until 300 cycles, Zn/Ti (1:3) exhibits significantly lower capacities (~507 mAh cm^{-3} after 300 cycles) than Zn/Ti (1:1) (~1062 mAh·cm^{-3} after 300 cycles), indicating that an excessively high Ti content in Zn/Ti also leads to a reduced specific capacity of the electrode.

To further confirm the enhanced electrical conductivity of carbon-free Zn/Ti (11) in comparison with the Zn-TiC-C composite and pure Zn electrodes, we performed EIS measurements for the three different electrodes before and after 50 cycles at the same current density. As shown in Fig. 7 along with equivalent circuit model, the depressed semicircle in the medium-to-high-frequency region consists primarily of the interfacial charge-transfer impedance (R_{ct}), although the high-frequency SEI film impedance (R_s)

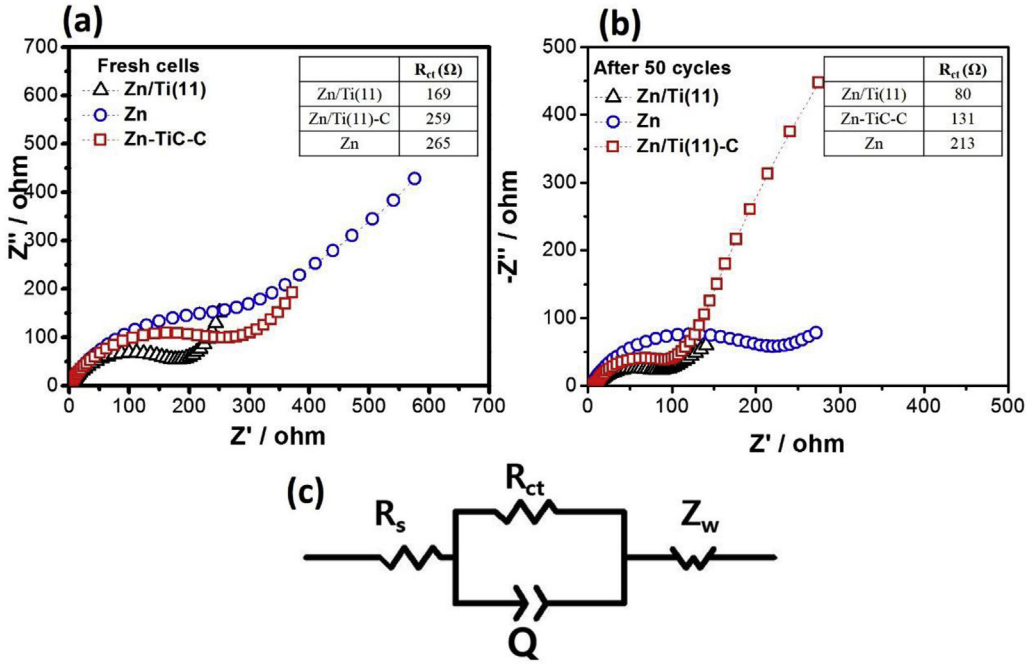

Fig. 7. EIS spectra of carbon-free Zn/Ti (11), Zn-TiC-C, and pure Zn (a) before and (b) after 50 cycles along with equivalent circuit model.

also contributes to its electrochemical impedance. The charge transfer resistance (R_{ct}) and SEI film resistance (R_s) are estimated by applying the simplified equivalent circuit (as shown in Fig. 7c) and fitting this model to the Nyquist plots where the diameters of the first and second semicircles correspond to R_s and R_{ct}, respectively [39]. The values of R_{ct} of electrodes after 50 cycles are 80, 131, and 213 Ω for carbon-free Zn/Ti (11), Zn-TiC-C, and pure Zn, respectively, which are much smaller than those of before cycle electrodes of 169, 259, 265 Ω, respectively. This could be attributed to the activation process of those electrodes after cycling compared to fresh cells. On the other hand, as compared to Zn-TiC-C and pure Zn electrodes, carbon-free Zn/Ti (11) shows the lowest charge-transfer impedance in both cases of before and after cycles. These results indicate that the introduction of Zn_xTi_y as a conductive matrix provides effective electron pathways into the active particles, thereby enhancing the electronic conductivity. However, the pure Zn electrode shows significantly greater charge-transfer resistance, resulting from the large volume changes during repeated cycling that leads to electrode pulverization and loss of electrical contacts with the current collector after 50 cycles. These results are consistent with the long-term cyclic performance and rate capability, as shown in Fig. 6.

Finally, Fig. 8 shows the *ex situ* SEM images of carbon-free Zn/Ti (11) and pure Zn electrode before and after 50 cycles. It can be seen

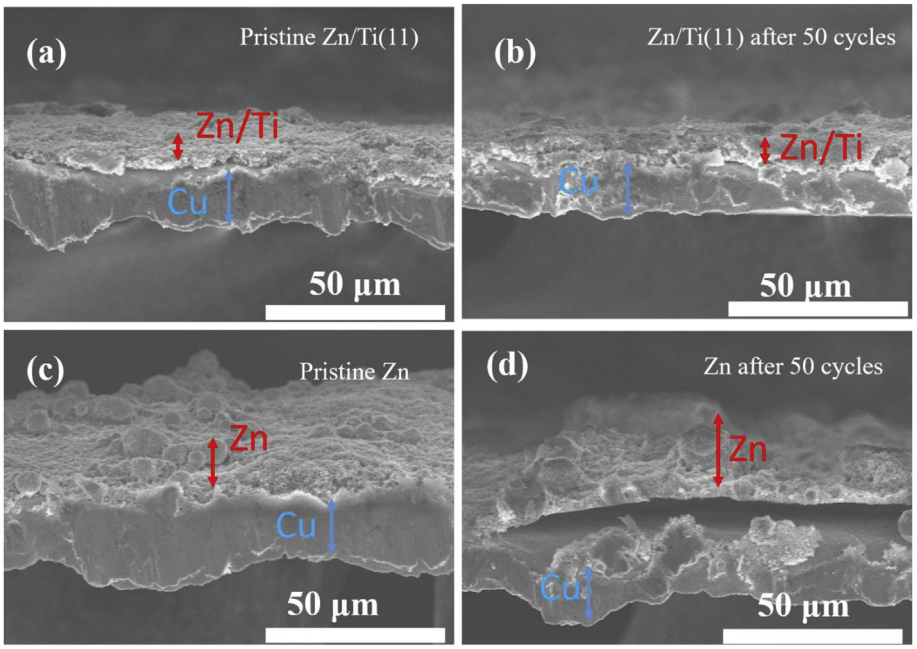

Fig. 8. *Ex situ* SEM images of pristine and 50 cyclized electrodes of (a–b) carbon-free Zn/Ti (11) and (c–d) pure Zn.

that the original morphology has been primarily maintained for the carbon-free Zn/Ti (11) electrode after 50 cycles, while the pure Zn electrode film exhibits significant aggregations, even the peeling-off from the current collector, resulting in the loss of electrical contacts with the current collector, poor reversibility, and eventually rapid capacity decay. This result explains the excellent electrochemical performances of carbon-free intermetallic Zn/Ti (11) alloys over pure Zn anodes for LIBs.

4. Conclusions

The performance enhancement of carbon-free intermetallic zinc titanium alloy anode was demonstrated for LIBs for the first time. The primary reason for this improved performance is the presence of stable and cohesive Zn_xTi_y intermetallic phases that are formed via thermal-treatment followed by HEMM. These phases act as an effective buffering matrix for Zn during the cycling. The formation of the intermetallic Zn_xTi_y phase without carbon contributed to the superior cycle life and rate capability because of the buffering role against Zn volume changes and the conductivity enhancement. In addition, the Zn-Zn_xTi_y electrode demonstrates improved gravimetric and volumetric capacity because of no capacity contribution from carbon and high tap density. Overall, the carbon-free intermetallic Zn/Ti (11) alloy can be seen as a new promising anode for next-generation energy storage applications.

Acknowledgments

This research was supported by the Basic Science Research Program through the National Research Foundation of Korea (NRF) funded by the Ministry of Education (NRF-2016R1D1A1B03931903). This work was supported by the Korea Institute of Energy Technology Evaluation and Planning (KETEP) and the Ministry of Trade, Industry & Energy (MOTIE) of the Republic of Korea (No. 20162010104190).

Appendix A. Supplementary data

Supplementary data to this article can be found online at https://doi.org/10.1016/j.electacta.2019.01.182.

References

[1] M. Armand, J.M. Tarascon, Building better batteries, Nature 451 (2008) 652–657. http://doi.org/10.1038/451652a.
[2] D. Applestone, S. Yoon, A. Manthiram, Mo_3Sb_7-C composite anodes for lithium-ion batteries, J. Phys. Chem. C 115 (2011) 18909–18915. http://doi.org/10.1021/jp206012v.
[3] L.W. Ji, Z. Lin, M. Alcoutlabi, X.W. Zhang, Recent developments in nanostructured anode materials for rechargeable lithium-ion batteries, Energy Environ. Sci. 4 (2011) 2682–2699. http://doi.org/10.1039/c0ee00699h.
[4] J.M. Tarascon, M. Armand, Issues and challenges facing rechargeable lithium batteries, Nature 414 (2001) 359–367. http://doi.org/10.1038/35104644.
[5] N.Q. Hai, S.H. Kwon, H. Kim, I.T. Kim, S.G. Lee, J. Hur, High-performance MoS_2-based nanocomposite anode prepared by high-energy mechanical milling: the effect of carbonaceous matrix on MoS_2, Electrochim. Acta 260 (2018) 129–138. http://doi.org/10.1016/j.electacta.2017.11.068.
[6] H. Kim, E.J. Lee, Y.K. Sun, Recent advances in the Si-based nanocomposite materials as high capacity anode materials for lithium ion batteries, Mater. Today 17 (2014) 285–297. http://doi.org/10.1016/j.mattod.2014.05.003.
[7] N.T. Hung, J. Bae, J.H. Kim, H.B. Son, I.T. Kim, J. Hur, Facile preparation of a zinc-based alloy composite as a novel anode material for rechargeable lithium-ion batteries, Appl. Surf. Sci. 429 (2018) 210–217. http://doi.org/10.1016/j.apsusc.2017.06.095.
[8] E. Allcorn, A. Manthiram, $FeSb_2$-Al_2O_3-C nanocomposite anodes for lithium-ion batteries, ACS Appl. Mater. Interfaces 6 (2014) 10886–10891. http://doi.org/10.1021/am500448f.
[9] H.H. Li, X.L. Wu, L.L. Zhang, C.Y. Fan, H.F. Wang, X.Y. Li, H.Z. Sun, J.P. Zhang, Q.Y. Yan, Carbon-free porous Zn_2GeO_4 nanofibers as advanced anode materials for high-performance lithium ion batteries, ACS Appl. Mater. Interfaces 8 (2016) 31722–31728. http://doi.org/10.1021/acsami.6b11503.
[10] M. Bian, Y. Yang, L. Tian, Carbon-free $Li_4Ti_5O_{12}$ porous nanofibers as high-rate and ultralong-life anode materials for lithium-ion batteries, J. Phys. Chem. Solid. 113 (2018) 11–16. http://doi.org/10.1016/j.jpcs.2017.10.006.
[11] K.J. Lee, S.H. Yu, J.J. Kim, D.H. Lee, J. Park, S.S. Suh, J.S. Cho, Y.E. Sung, $Si_7Ti_4Ni_4$ as a buffer material for Si and its electrochemical study for lithium ion batteries, J. Power Sources 246 (2014) 729–735. http://doi.org/10.1016/j.jpowsour.2013.08.033.
[12] J.B. Wu, Z.W. Zhu, H.W. Zhang, H.M. Fu, H. Li, A.M. Wang, H.F. Zhang, A novel Si/Sn composite with entangled ribbon structure as anode materials for lithium ion battery, Sci. Rep.-Uk 6 (2016). http://doi.org/10.1038/srep29356.
[13] A. Ladam, N. Bibent, C. Cenac-Morthe, L. Aldon, J. Olivier-Fourcade, J.C. Jumas, P.E. Lippens, One-pot ball-milling synthesis of a Ni-Ti-Si based composite as anode material for Li-ion batteries, Electrochim. Acta 245 (2017) 489–496. http://doi.org/10.1016/j.electacta.2017.05.093.
[14] H.J. Kwon, K.Y. Sohn, W.W. Park, Electrochemical properties of rapidly solidified Si-Ti-Ni(-Cu) base anode for Li-ion rechargeable batteries, Electron. Mater. Lett. 9 (2013) 859–863. http://doi.org/10.1007/s13391-013-6030-6.
[15] J.Y. Liu, W.K. Pang, T. Zhou, L. Chen, Y.G. Wang, V.K. Peterson, Z.Q. Yang, Z.P. Guo, Y.Y. Xia, Li2TiSiO5: a low potential and large capacity Ti-based anode material for Li-ion batteries, Energy Environ. Sci. 10 (2017) 1456–1464. http://doi.org/10.1039/c7ee00763a.
[16] X.Y. Wu, J. Miao, W.Z. Han, Y.S. Hu, D.F. Chen, J.S. Lee, J. Kim, L.Q. Chen, Investigation on $Ti_2Nb_{10}O_{29}$ anode material for lithium-ion batteries, Electrochem. Commun. 25 (2012) 39–42. http://doi.org/10.1016/j.elecom.2012.09.015.
[17] T.A. Yersak, S.B. Son, J.S. Cho, S.S. Suh, Y.U. Kim, J.T. Moon, K.H. Oh, S.H. Lee, An all-solid-state Li-ion battery with a pre-lithiated Si-Ti-Ni alloy anode, J. Electrochem. Soc. 160 (2013) A1497–A1501. http://doi.org/10.1149/2.086309jes.
[18] M.S. Park, G.X. Wang, Y.M. Kang, D. Wexler, S.X. Dou, H.K. Liu, Preparation and electrochemical properties of SnO2 nanowires for application in lithium-ion batteries, Angew. Chem. Int. Ed. 46 (2007) 750–753. http://doi.org/10.1002/anie.200603309.
[19] D.M. Seo, C.C. Nguyen, B.T. Young, D.R. Heskett, J.C. Woicik, B.L. Lucht, Characterizing solid electrolyte interphase on Sn anode in lithium ion battery, J. Electrochem. Soc. 162 (2015) A7091–A7095. http://doi.org/10.1149/2.0121513jes.
[20] W.J. Zhang, A review of the electrochemical performance of alloy anodes for lithium-ion batteries, J. Power Sources 196 (2011) 13–24. http://doi.org/10.1016/j.jpowsour.2010.07.020.
[21] X.D. Li, Y. Feng, M.C. Li, W. Li, H. Wei, D.D. Song, Smart hybrids of Zn_2GeO_4 nanoparticles and ultrathin g-C_3N_4 layers: synergistic lithium storage and excellent electrochemical performance, Adv. Funct. Mater. 25 (2015) 6858–6866. http://doi.org/10.1002/adfm.201502938.
[22] C.M. Park, H.J. Sohn, Black phosphorus and its composite for lithium rechargeable batteries, Adv. Mater. 19 (2007), 2465-+, http://doi.org/10.1002/adma.200602592.
[23] E. Allcorn, A. Manthiram, NiSb-Al_2O_3-C nanocomposite anodes with long cycle life for Li-ion batteries, J. Phys. Chem. C 118 (2014) 811–822. http://doi.org/10.1021/jp409223c.
[24] N.T. Hung, S.H. Park, J. Bae, Y.S. Yoon, J.H. Kim, H.B. Son, D. Lee, I.T. Kim, J. Hur, Sb-Al_xC_y-C nanocomposite alloy anodes for lithium-ion batteries, Electrochim. Acta 210 (2016) 567–574. http://doi.org/10.1016/j.electacta.2016.05.019.
[25] M.P. Bichat, J.L. Pascal, F. Gillot, F. Favier, Electrochemical lithium insertion in Zn_3P_2 zinc phosphide, Chem. Mater. 17 (2005) 6761–6771. http://doi.org/10.1021/cm0513379.
[26] A. Dailly, J. Ghanbaja, P. Willmann, D. Billaud, Electrochemical insertion of lithium into graphite-zinc composites, J. Appl. Electrochem. 34 (2004) 885–890. http://doi.org/10.1023/B:JACH.0000040438.91141.ba.
[27] Y. Hwa, J.H. Sung, B. Wang, C.M. Park, H.J. Sohn, Nanostructured Zn-based composite anodes for rechargeable Li-ion batteries, J. Mater. Chem. 22 (2012) 12767–12773. http://doi.org/10.1039/c2jm31776a.
[28] N. Yan, F. Wang, H. Zhong, Y. Li, Y. Wang, L. Hu, Q.W. Chen, Hollow porous SiO_2 nanocubes towards high-performance anodes for lithium-ion batteries, Sci. Rep.-Uk 3 (2013). http://doi.org/10.1038/srep01568.
[29] H.J. Tian, F.X. Xin, X.L. Wang, W. He, W.Q. Han, High capacity group-IV elements (Si, Ge, Sn) based anodes for lithium-ion batteries, J Materiomics 1 (2015) 153–169. http://doi.org/10.1016/j.jmat.2015.06.002.
[30] C.M. Park, H.J. Sohn, Tetragonal zinc diphosphide and its nanocomposite as an anode for lithium secondary batteries, Chem. Mater. 20 (2008) 6319–6324. http://doi.org/10.1021/cm800632f.
[31] C.M. Park, H.J. Sohn, Quasi-intercalation and facile amorphization in layered ZnSb for Li-ion batteries, Adv. Mater. 22 (2010) 47–52. http://doi.org/10.1002/adma.200901427.
[32] W. Qi, J.G. Shapter, Q. Wu, T. Yin, G. Gao, D.X. Cui, Nanostructured anode materials for lithium-ion batteries: principle, recent progress and future perspectives, J. Mater. Chem. 5 (2017) 19521–19540. http://doi.org/10.1039/c7ta05283a.
[33] S.O. Kim, A. Manthiram, High-performance Zn-TiC-C nanocomposite alloy anode with exceptional cycle life for lithium-ion batteries, ACS Appl. Mater. Interfaces 7 (2015) 14801–14807. http://doi.org/10.1021/acsami.5b03110.
[34] Y. Xiao, J.Y. Hwang, Y.K. Sun, Micro-intertexture carbon-free iron sulfides as advanced high tap density anodes for rechargeable batteries, ACS Appl. Mater. Interfaces 9 (2017) 39416–39424. http://doi.org/10.1021/acsami.7b13239.
[35] L. Zhao, Y.S. Hu, H. Li, Z.X. Wang, L.Q. Chen, Porous $Li_4Ti_5O_{12}$ coated with N-

doped carbon from ionic liquids for Li-ion batteries, Adv. Mater. 23 (2011) 1385–1388. http://doi.org/10.1002/adma.201003294.
[36] X.B. Cheng, R. Zhang, C.Z. Zhao, F. Wei, J.G. Zhang, Q. Zhang, A review of solid electrolyte interphases on lithium metal anode, Adv. Sci. 3 (2016). http://doi.org/UNSP150021310.1002/advs.201500213.
[37] G. Ghosh, S. Delsante, G. Borzone, M. Asta, R. Ferro, Phase stability and cohesive properties of Ti-Zn intermetallics: first-principles calculations and experimental results, Acta Mater. 54 (2006) 4977–4997. http://doi.org/10.1016/j.actamat.2006.04.038.
[38] J. Leibowitz, E. Allcorn, A. Manthiram, SnSb-TiC-C nanocomposite alloy anodes for lithium-ion batteries, J. Power Sources 279 (2015) 549–554. http://doi.org/10.1016/j.jpowsour.2015.01.055.
[39] S.Y. Son, J. Hur, K.H. Kim, H.B. Son, S.G. Lee, I.T. Kim, SnTe-TiC-C composites as high-performance anodes for Li-ion batteries, J. Power Sources 365 (2017) 372–379. http://doi.org/10.1016/j.jpowsour.2017.08.105.
[40] I.T. Kim, E. Allcorn, A. Manthiram, High-performance FeSb-TiC-C nanocomposite anodes for sodium-ion batteries, Phys. Chem. Chem. Phys. 16 (2014) 12884–12889. http://doi.org/10.1039/c4cp01240b.
[41] D. Saikia, T.H. Wang, C.J. Chou, J. Fang, L.D. Tsai, H.M. Kao, A comparative study of ordered mesoporous carbons with different pore structures as anode materials for lithium-ion batteries, RSC Adv. 5 (2015) 42922–42930. http://doi.org/10.1039/c5ra05168a.
[42] S. Yoon, A. Manthiram, Nanoengineered Sn-TiC-C composite anode for lithium ion batteries, J. Mater. Chem. 20 (2010) 236–239. http://doi.org/10.1039/b919116j.
[43] L. Liu, M. An, P. Yang, J. Zhang, Superior cycle performance and high reversible capacity of SnO_2/graphene composite as an anode material for lithium-ion batteries, Sci. Rep. 5 (2015) 9055. http://doi.org/https://doi.org/10.1038/srep09055.
[44] H. Guo, X. Song, J. Zheng, F. Pan, Excess lithium storage in $LiFePO_4$-Carbon interface by ball-milling, Functional Materials Letters 9 (2016) 1650053. http://doi.org/https://doi.org/10.1142/S1793604716500533.
[45] Y. Duan, B. Zhang, J. Zheng, J. Hu, J. Wen, D.J. Miller, P. Yan, T. Liu, H. Guo, W. Li, Excess Li-ion storage on reconstructed surfaces of nanocrystals to boost battery performance, Nano Lett. 17 (2017) 6018–6026. http://doi.org/10.1021/acs.nanolett.7b02315.
[46] F.J. Sonia, M.K. Jangid, B. Ananthoju, M. Aslam, P. Johari, A. Mukhopadhyay, Understanding the Li-storage in few layers graphene with respect to bulk graphite: experimental, analytical and computational study, J. Mater. Chem. 5 (2017) 8662–8679. http://doi.org/10.1039/c7ta01978e.